POLITECNICO DI TORINO
Repository ISTITUZIONALE

Powder bed fusion with electron beam of Ti4822: assessing the benefits of contour on surface topography and part precision

Original
Powder bed fusion with electron beam of Ti4822: assessing the benefits of contour on surface topography and part precision / Rizza, G., Minetola, P., Galati, M.. - In: PROGRESS IN ADDITIVE MANUFACTURING. - ISSN 2363-9512. - ELETTRONICO. - (2026). [10.1007/s40964-026-01569-z]

Availability:
This version is available at: 11583/3009838 since: 2026-04-13T14:43:41Z

Publisher:
Springer Science and Business Media Deutschland GmbH

Published
DOI:10.1007/s40964-026-01569-z

Terms of use:

This article is made available under terms and conditions as specified in the corresponding bibliographic description in the repository

Publisher copyright

(Article begins on next page)

12 November 2026

Progress in Additive Manufacturing
https://doi.org/10.1007/s40964-026-01569-z

RESEARCH

Powder bed fusion with electron beam of Ti4822: assessing the benefits of contour on surface topography and part precision

Giovanni Rizza[1] · **Paolo Minetola**[1] · **Manuela Galati**[1]

Received: 27 March 2025 / Accepted: 28 January 2026
© The Author(s) 2026

Abstract
The titanium aluminide alloy γ-TiAl Ti48Al2Cr2Nb (Ti4822) is, to a great extent, produced by powder bed fusion with electron beam melting (PBF-EB). Owing to the high working temperature and the vacuum environment, PBF-EB for Ti4822 maintains phase stability and minimises residual stresses. The standard melting procedure of PBF-EB considers the melt of the section in two steps: the contour of the area first and then the inner area through a hatching strategy. Despite this standard, Ti4822 is today processed only by melting the inner area of the sliced section through hatching. The reasons for such strategy or benefits in terms of, e.g. the component quality, are not clear. This paper covers this literature gap, showing the differences between a two-step strategy and a one-step using only hatching. Reference artefacts were produced using a PBF-EB machine and γ-TiAl Ti48Al2Cr2Nb alloy. The surface topography, dimensional accuracy and geometrical tolerances of the two strategies were observed and compared. The results provide preliminary guidelines for correcting and adjusting the geometry according to the PBF-EB capabilities. The contour in the two-step strategy significantly improves the surface roughness by modifying the topography of the vertical surfaces. On the other hand, the one-step strategy guarantees the production of more dimensionally accurate features for some size classes. The two-step strategy can better control the part dimensions but requires a longer time.

Keywords Electron beam melting · Melting strategy · Topography · Dimensions · International tolerance

1 Introduction

The building conditions of the powder bed fusion with electron beam (PBF-EB) additive manufacturing process enable the production of materials that are difficult to process using traditional or other additive manufacturing techniques. One such example is the intermetallic γ titanium aluminide alloy [1]. This advantage is guaranteed by the high build process temperature and the vacuum environment in the build chamber [2]. The vacuum level is approximately 10^{-5} mbar, sufficient to prevent the backscatter of the electrons by the air molecules and allow the material to be processed without the risk of oxygen or nitrogen pickup [3]. With these processing conditions, γ-TiAl offers remarkable specific properties of strength, Young modulus and creep resistance, particularly when compared to nickel alloys [2]. These properties make γ-TiAl intermetallic appealing candidates to replace heavy Ni-based superalloys. Industrial examples are the low-pressure turbine blades of IV and V stages of the GE9X, the largest and most powerful commercial aircraft engine [4]. For this application, Ti48Al2Cr2Nb (Ti4822) is used. Behind the aerospace application, this alloy processed by PBF-EB also showed potential for biomedical applications [5].

The granulometry of the Ti4822 powder processed by PBF-EB is typically in the range of 50 µm - 150 µm, and the processing temperature in the build chamber for the whole duration of the build is maintained between 1050 °C and 1100°C [2]. This temperature is kept approximately constant thanks to the preheating of each layer that precedes

✉ Giovanni Rizza
giovanni.rizza@polito.it

Paolo Minetola
paolo.minetola@polito.it

Manuela Galati
manuela.galati@polito.it

[1] Department of Management and Production Engineering (DIGEP), Integrated Additive Manufacturing Center (IAM@PoliTo), Polytechnic University of Turin, C.so Duca degli Abruzzi, 24, 10129 Turin, Italy

Published online: 02 April 2026

the section melting [6]. The layer thickness for the slicing parameter for this alloy typically ranges between 0.050 mm and 0.100 mm [7], which corresponds to the lowering of the start plate at each layer. However, to compensate for the changes in the dimension of the powder layer during melting, the amount of deposited material is larger. This practically means a distributed layer thickness of around 0.200 mm, between 2–3 times the slicing layer thickness [8]. During the preheating, the powder is sintered [9], improving the heat transfer and reducing the cooling rate of the melt pool [2]. The studies addressing the production and analysis of Ti4822 by PBF-EB processed such material by melting the section obtained from the slicing operation on the 3D CAD model in one single step using parallel lines [10–19]. This strategy is usually referred to as hatching [3, 20]. The distance between two parallel lines is the line offset and is usually selected to allow a certain remelting of the previous line to ensure material continuity [2]. In addition, the direction of the lines is rotated at each layer to improve the homogeneity of the material [3, 20].

To the best of the authors' knowledge, Ti4822 has never been processed using the most common two-step melting strategy of the PBF-EB well established for other materials such as Ti6Al4V [21, 22], Ti6Al2Sn4Zr2Mo [23], Inconel 718 [24] or H13 stainless steel [25]. This strategy consists of two melting steps: the contour first and the inner or hatch after [3, 20]. Figure 1 shows schematically the melting strategy for contour (Fig. 1a) and hatch (Fig. 1b). Figure 1 also shows the result of contour (Fig. 1a) and hatch (Fig. 1b) on produced components. The contour employs a highly distinctive melting strategy known as the Multibeam™. During Multibeam™, the PBF-EB machine control rapidly moves the electron beam in different contour locations, simultaneously activating several melt pools [26].

The literature on other materials such as Ti6Al4V [22], Ti6242 [23] or alloy 718 [27] suggests that the use of contour previously to the hatching of the inner area affects only the surface roughness of the components, which is smaller for components produced using contours [27]. The reason for this difference is thermal, and it is due to the larger amount of energy delivered when melting the hatch than when melting the contour. A larger amount of energy produces a larger melt pool with a consequent effect on the surface roughness [27]. However, given the stringent requirements typically associated with γ-TiAl components in automotive or aerospace industries, such improvements may still be insufficient, necessitating additional machining operations. Moreover, the use of the contour strategy may presumably alter the heat distribution from the melted section to the sintered powder, potentially impacting the dimensional and shape accuracy of the part. Despite diverse works in the literature show the part quality issues associated with the PBF-EB production, typically for titanium alloys, such as Ref. [23, 28–31], all of these works are only based on the use of the two-step strategy and no comparison has been made with respect of the one-step strategy. This paper covers this literature gap, investigating the differences between two-step and one-step strategies and highlighting the benefits of defining such strategies to produce Ti4822. Two artefacts were produced using the standard two-step and the one-step strategy. A comparison of the melting strategies was made considering the topography of the surfaces and the dimensional and geometrical tolerances.

2 Materials and methods

2.1 Geometry of the artefacts

To investigate the effect of the melting strategy, this work adopts two portions of the benchmark proposed by Minetola et al. [32] and relative procedure for the measurements

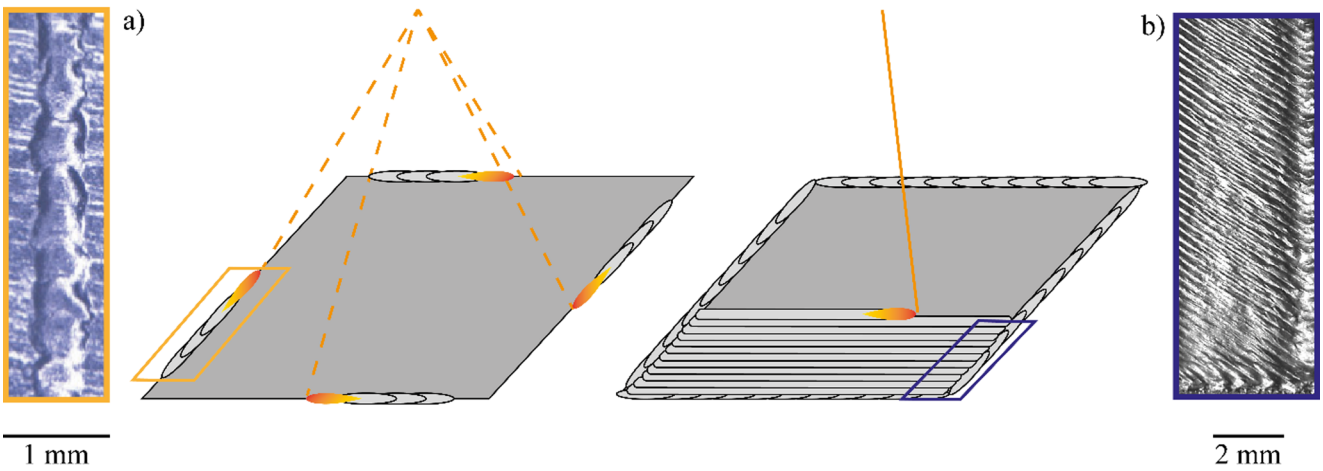

Fig. 1 Melting strategies in PBF-EB. **a** Contour melting and **b** hatch melting

developed according to the standard ISO 286:1988 [33] and ISO 286-1:2010 [34]. Such procedure has been showed to be robust across several manufacturing processes [35–37] for polymers and metals. The benchmark reference part is available as open access here [38]. Figure 2 shows the artefacts 1 and 2 adopted in this work and the position on the build start plate.

The overall size of artefact 1 are 110 mm × 25 mm × 33 mm, while artefact 2 has an overall size of 55 mm × 55 mm × 21 mm. Artefacts 1 and 2 include features with sizes that are comprised in the basic size ranges of the ISO 286:1988 [33] and ISO 286-1:2010 [34]: from 1 to 3 mm, from 3 to 6 mm, from 6 to 10 mm, from 10 to 18 mm, from 18 to 30 mm, from 30 to 50 mm, from 50 to 80 mm and from 80 to 120 mm. All these features are built on a 5 mm thick supporting plate (highlighted in green in Fig. 2). Each set of features is named with an alphabetic index, as shown in Fig. 2 and described below.

On one side of artefact 1, there are seven rectangular steps (ST in Fig. 2) with dimensions 4 mm × 15 mm. The height of these steps is 1 mm, 3 mm, 6 mm, 10 mm, 15 mm, 21 mm and 28 mm. The central portion of this artefact includes a rectangular block with dimensions 20 mm × 46 mm × 24 mm. This block contains seven rectangular slots (SL in Fig. 2) with dimensions 5 mm × 15 mm. The depth of these slots is the same as the steps, except for the slot 3 mm deep, which is repeated two times. One side of this central block includes five planes tilted at different angles with respect to the vertical (TP in Fig. 2). The first is vertical, the second is tilted at 2 degrees, the third at 4.5 degrees, the fourth at 7 degrees and the fifth at 9 degrees. Artefact 1 also contains seven rectangular blocks (BL in Fig. 2) with dimensions of 4 mm × 15 mm separated by a 1 mm gap. The height of these blocks is the same as the steps.

Artefact 2 contains two truncated cones with a circular base (TC1 in Fig. 2), one inside the other. The larger base of the external cone has a diameter of 20 mm, while the smaller base has a diameter of 13.6 mm. The height of this cone is 12 mm. The larger base of the inner cone has a diameter of 10 mm, while the smaller one has a diameter of 6.5 mm. The height of this cone is 10 mm. Artefact 2 also contains a series of coaxial cylinders (CC1 in Fig. 2). The larger cylinder has a diameter of 24 mm, while the smaller cylinder on top has a diameter of 17 mm. This feature contains two other internal cylinders with a diameter of 7 mm, the one on top and 5 mm, the one at the bottom. Each cylinder has a height of 8 mm. The last features are two series of quarters of convex and concave spheres (SP1 and SP2 in Fig. 2). The spheres of SP1 have a diameter of 24 mm, while the spheres of SP2 have a diameter of 16 mm. Artefacts 1 and 2 together allow the evaluation of more than one thousand dimensions in the ISO ranges of 1 mm and 120 mm. The arrangement of the features also allows the evaluation with a coordinate measuring machine (CMM) using only one positioning of the sample and a probe of 2 mm in diameter.

2.2 Production

The PBF-EB machine Arcam A2X (Colibrium additive a GE aerospace company, Mölnlycke, Sweden) was adopted to produce artefacts 1 and 2. The machine was manually calibrated. As mentioned above, the material adopted was the intermetallic Ti48Al2Cr2Nb alloy (Ti4822). Table 1 reports the composition of the powder. The granulometry was comprised between 45 µm and 150 µm with 66.9% of the powder particles with a diameter comprised in the range 45–105 µm and 29.9% in the range 105–150 µm. According to the literature [7], the layer thickness was selected as equal to 90 µm.

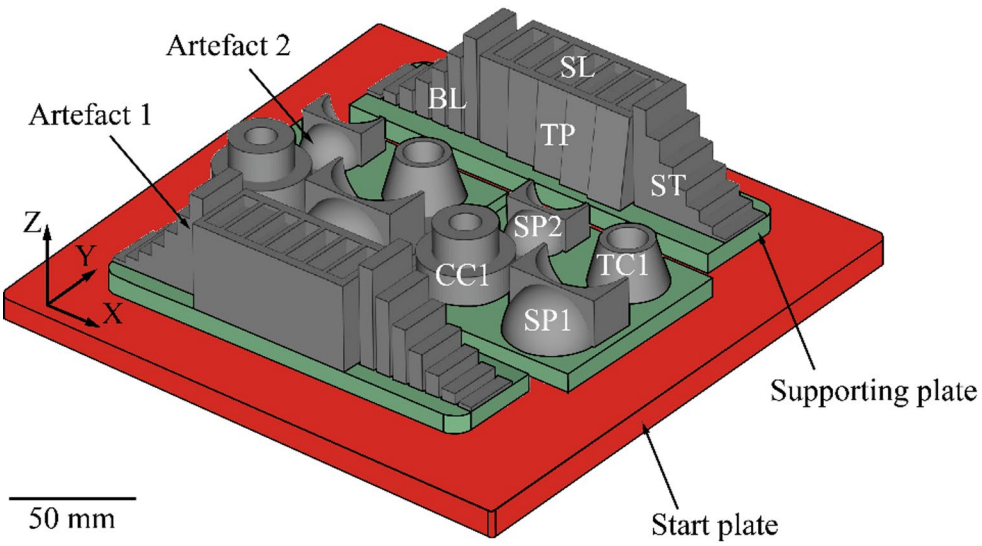

Fig. 2 Artefacts adopted to investigate the effect of the melting strategy and the relative position on the start plate. The quotes of the overall size are expressed in mm. The z-axis corresponds to the build direction

Table 1 Chemical composition of the Ti48Al2Cr2Nb alloy

Element	Al	Cr	Nb	Fe	C	O	N	H
Wt%	34.2	2.5	4.7	0.03	0.01	0.1	<0.01	<0.01

Table 2 Process parameters adopted to melt the contour with Multibeam™ and hatch

Melt strategy	Scan speed [mm/s]	Focus offset [mA]	Beam current [mA]	Number of spots	Number of contours	Contour offset [mm]
Outer contour with Multibeam™	440	6	5	40	1	0.25
Inner contour with Multibeam™	800	6	10.2	15	2	0.25
	Speed function	Focus offset [mA]	Beam current max [mA]	Reference length [mm]	Reference current [mA]	Line offset [mm]
Hatch	40	15	20	18	7	0.3

Two replicas of artefacts 1 and 2 were produced: one replica for each melt strategy. As a reminder, the one-step strategy refers to the typical approach for processing Ti4822, involving only the hatching. In contrast, the two-step strategy follows the same parameters as the one-step strategy for the inner area, but it is preceded by an outer contour and two inner contours, which are executed using a Multibeam™ strategy. Table 2 reports the process parameters adopted to melt contour with Multibeam™ and hatch for the parts produced with the two-step strategy. The artefacts produced with the one-step strategy were produced using the parameters for the hatch reported in Table 2. No scaling factor was applied to the nominal geometries. The four samples were produced in one build to ensure the same temperature conditions. The total time required to build the samples was 6 h and 54 min. At the end of the production, the samples were cleaned in a powder recovery system according to the standard procedure [3, 39] in which the breakaway powder was sandblasted using the same powder used in the PBF-EB process. No heat treatments or other post-process operations were performed on the artefacts produced. After the cleaning, the samples were characterised topographically and dimensionally as described in the following sections.

2.3 Topography characterisation

The topography was investigated by inspecting peaks and valleys to highlight the differences in the melting strategy adopted. The topography of the samples was obtained through a structured light scanner ATOS compact scan (Carl Zeiss GOM Metrology GmbH, Braunschweig, Germany). The maximum resolution of the scanner is 0.018 mm. The cloud of points acquired by the scanner was cleared by the points that do not belong to the artefact investigated and converted into an STL file using the software GOM inspect 2021 (Carl Zeiss GOM Metrology GmbH, Braunschweig, Germany), with no post-process. The software MountainsLab (Digital Surf, Besançon, France) was adopted to inspect topography characteristics. The STL file of the artefacts was imported into the software, and horizontal and vertical surfaces were selected for the characterisation. Horizontal surfaces are all the surfaces parallel to the start plate of the sample upon which the features are attached. Vertical surfaces are orthogonal to the supporting plate of the sample. Since the artefacts are attached to the start plate of the machine, the vertical surfaces are aligned with the build direction. Figure 3 shows for artefact 1 (Fig. 3a) and artefact 2 (Fig. 3b) the location of the vertical and horizontal surfaces investigated. The location for the investigation was maintained the same to be consistent during the inspection of all artefacts. Vertical surfaces were investigated considering an area with dimensions of 10.5 mm × 10.5 mm. Horizontal surfaces were investigated considering an area of 7.5 mm × 7.5 mm. The software MountainsLab was adopted to create the false colour height maps and to calculate the area roughness parameters, among which the average surface roughness (Sa) and the maximum height of the surface (Sz) were chosen as representative of the surface characteristics. The horizontal surfaces were also inspected using the stereomicroscope Leica S9i (Leica Microsystems GmbH, Wetzlar, Germany), and the software Fiji 1.54 [40] was adopted to evaluate the width of the melt tracks on the top surface. Figure 3b also shows the location of the area inspected with the stereomicroscope.

2.4 Dimensional and geometrical analysis

The dimensional accuracy was investigated by a CMM Altera S (LK Metrology Ltd., Derby, England). This machine has an accuracy envelope with a maximum permissible error for length measuring of 1.8 + L/400. Each artefact was measured three times, and the average measure was adopted for the analysis. The measures taken through the CMM were adopted to evaluate the standard tolerance factor according to the ISO guidelines [33]. The standard tolerance classes, from IT5 to IT18, for measures up to 500 mm, are a function of the standard tolerance factor i described by Eq. 1

$$i = 0.45\sqrt[3]{D} + 0.001D \quad (1)$$

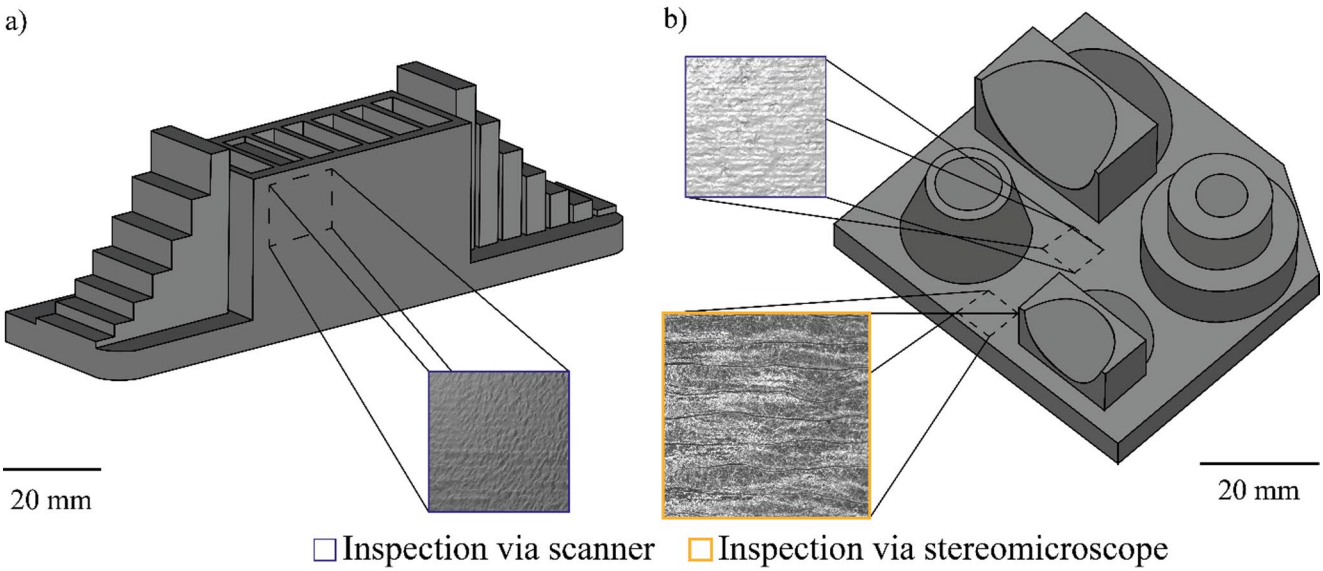

Fig. 3 Location of the areas for the surface topography characterisation. **a** Location for topography characterisation of vertical surfaces. **b** Location of the surface for characterisation of the horizontal surface and location of the melt track inspection location with the stereomicroscope

Table 3 Standard tolerance factors for each basic size

Range		Basic size							
Above	D_1 (mm)	1	3	6	10	18	30	50	80
Up to and including	D_2 (mm)	3	6	10	18	30	50	80	120
Standard tolerance factor	i (μm)	0.542	0.733	0.898	1.083	1.307	1.561	1.856	2.173

where $D = \sqrt{D_1 D_2}$ and D_1 and D_2 are the lower and the upper limits of the basic size range. Table 3 reports the value of the standard tolerance factor i calculated for each size range given by the ISO standard.

Table 4 reports the formulas adopted to assign a standard tolerance grade (IT) to a measure. This is assigned according to the number of times (n) the tolerance factor (i) fits the dimensional deviation of the measure from the nominal measure. The parameter n is evaluated according to Eq. 2.

$$n = 1000\ \frac{|D_n - D_m|}{i} \tag{2}$$

where D_n and D_m represent the nominal and the measured dimensions, respectively.

As an example, to clarify the use of Eqs. 1 and 2 and Tables 3 and 4, assuming a nominal dimension $D_n = 40$ mm and a measured dimension $D_m = 40.250$, the standard tolerance factor for this dimension is $i = 1.561$ μm (from Table 3 and Eq. 1) and the parameter $n = 160.15$ (Eq. 2). With this value of n, the dimension can be classified as an IT13. In order to be classified as IT 12, a measure should have a deviation between 100 i (with $n = 100$) and 160 i (with $n = 160$).

Considering all the features of the artefacts 1 and 2, n will have a distribution in each basic ISO range size. In this work, the 95th percentile is assumed as the maximum error when producing a feature in the specific range size of Table 3.

Besides the dimensional accuracy, the measures taken with CMM were adopted to evaluate the geometric dimensioning and tolerancing (GD&T). In particular, the following factors were investigated:

- perpendicularity
- cylindricity
- angle of the planes
- flatness of the planes for horizontal (parallel to the start plate), vertical (parallel to the build direction) and tilted with respect to the vertical planes
- parallelism between horizontal and vertical planes

2.5 Production time efficiency

To evaluate the differences in the production time between the two melting strategies, two ad-hoc builds were designed, containing only one replica of the artefact two. Only one melting strategy at one time was considered. The production time was estimated using the EBM control of the machine. The simulator calculates solely the time required for preheating, the melting of the cross-section and the eventual post-heating/cooling at each layer. From the calculation, the

Table 4 Formulas to assign the standard tolerance (IT) grade to a measure, according to his deviation from the nominal

Basic size [mm]		Standard tolerance grades												
		IT 5	IT 6	IT 7	IT 8	IT 9	IT 10	IT 11	IT 12	IT 13	IT 14	IT 15	IT 16	IT 17	IT 18
		Standard tolerance [µm]													
Above	Up to														
1 mm	500 mm	7i	10i	16i	25i	40i	64i	100i	160i	250i	400i	640i	1000i	1600i	2500i

time for the powder ranking is neglected since it is fixed and independent from the melted material.

3 Results and discussion

Figure 4 shows the produced samples after cleaning by the sandblasting process, using the same material as that used for production, in the powder recovery system. It also allows a visual comparison between the artefacts produced with the one-step and the two-step strategy.

For the production efficiency evaluation, the time calculated to produce samples with a two-step strategy was 2 h and 50 min, while the time calculated to produce the artefacts with the one-step strategy was 2 h and 37 min. As expected, the use of an additional phase makes the process slower and, in this case, the one-step strategy is approximately 8% faster than the two-step strategy. Although the difference may seem negligible, it is important to note that the time for the two-step strategy depends on the geometry, as well as the quantity and length of the perimeters in the components. In this case, the small size of the artefact explains the observed difference.

3.1 Surface topography

Figure 5 shows a detailed image of the convex sphere SP1 of artefact 2 produced with the two-step strategy (Fig. 5a) and with the one-step strategy (Fig. 5b). The surface produced with the one-step strategy (Fig. 5b) shows the presence of the layers, with the stair-stepping effect clearly visible. In the case of the two-step strategy, the stair stepping and the layers are visible for the highest section of the sphere, where the molten cross section becomes small (Fig. 5a).

Figure 6 shows the results of the topography analysis on vertical surfaces of artefact 1 produced with the two-step strategy (Fig. 6a–c) and the one-step strategy (Fig. 6d–f). As can be observed, the topography is substantially different, which is highlighted in the false colour maps of Fig. 6c, f. The first evidence is that the roughness of the surface is significantly affected by the contour. The surface melted with a two-step strategy is more regular with a less evident staircase effect due to the slicing operation. This evidence is confirmed quantitatively by the areal surface roughness measurements. The surface produced with the two-step strategy (Fig. 6c) is characterised by Sa = 31.4 µm, Sz = 331.4 µm, Sv = 202.5 µm and Sp = 128.9 µm. On the other hand, the surface produced with the one-step strategy is characterised by Sa = 54 µm, Sz = 499 µm, Sv = 207.7 µm and Sp = 291.3 µm. The higher values of Sa and Sz for the surfaces produced with the one-step strategy measure the larger number of peaks and valleys. Moreover, considering

Fig. 4 Samples produced using the one-step and the two-step strategy

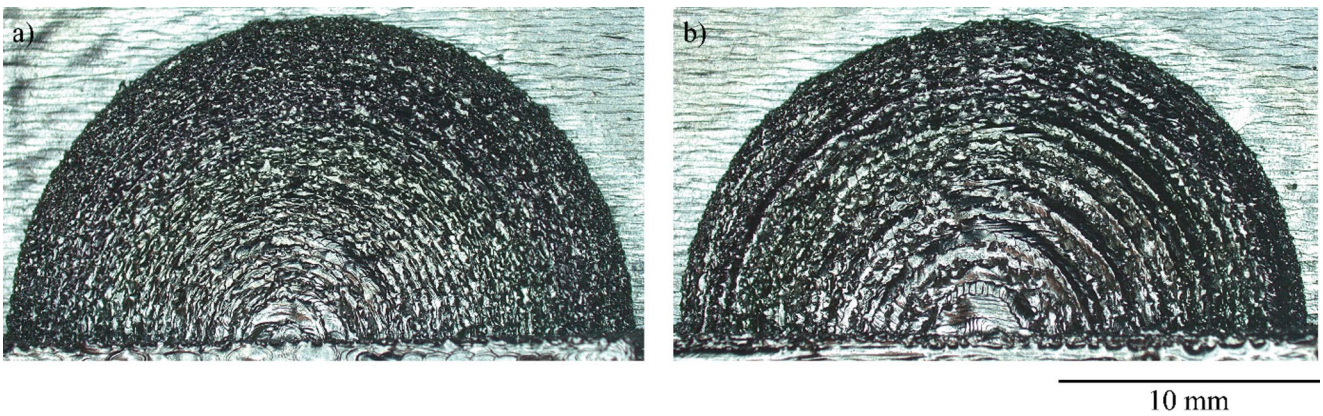

Fig. 5 Detailed image of the convex sphere SP1 of artefact 2 produced with two-step (**a**) and one-step (**b**) melting strategy

the values of Sv and Sp for the two melt strategies, the two-step strategies produced surfaces with a significantly reduced Sp. In contrast, the values of Sv are similar. This indicates that the two-step strategy produces surfaces with smaller values of surface roughness by removing the protruding peaks. The presence of the large peaks on the surfaces produced with the one-step strategy may be due to the fluid dynamics in the melt track. When melting a track, the Marangoni flow and recoil pressure in the melt pool produce a depression at the tip of the melt pool and the accumulation of material at the tail that is visible as peaks on the vertical surfaces produced with the one-step strategy. On the other hand, the peaks are smaller in the two-step strategy because the presence of the solid contour mitigates the material accumulation at the tail of the melt pool.

Despite this significant difference, both the surfaces produced with a one-step and two-step melting strategy are characterised by the peaks and valleys on the vertical surfaces that repeat approximately every 720 µm along the build direction. The presence of this pattern may be due to the rotation of an unknown angle of the hatch direction at every layer, which repeats after a certain number of layers. Since the layer thickness adopted was 90 µm, this suggests the same direction of the hatching lines is occurring every eight layers and a rotation of the hatch direction of 45° per layer.

Figure 7 shows the topography analysis of the horizontal surfaces. The topography of these surfaces does not show a substantial difference between the two melt strategies. The horizontal surface produced with a two-step strategy

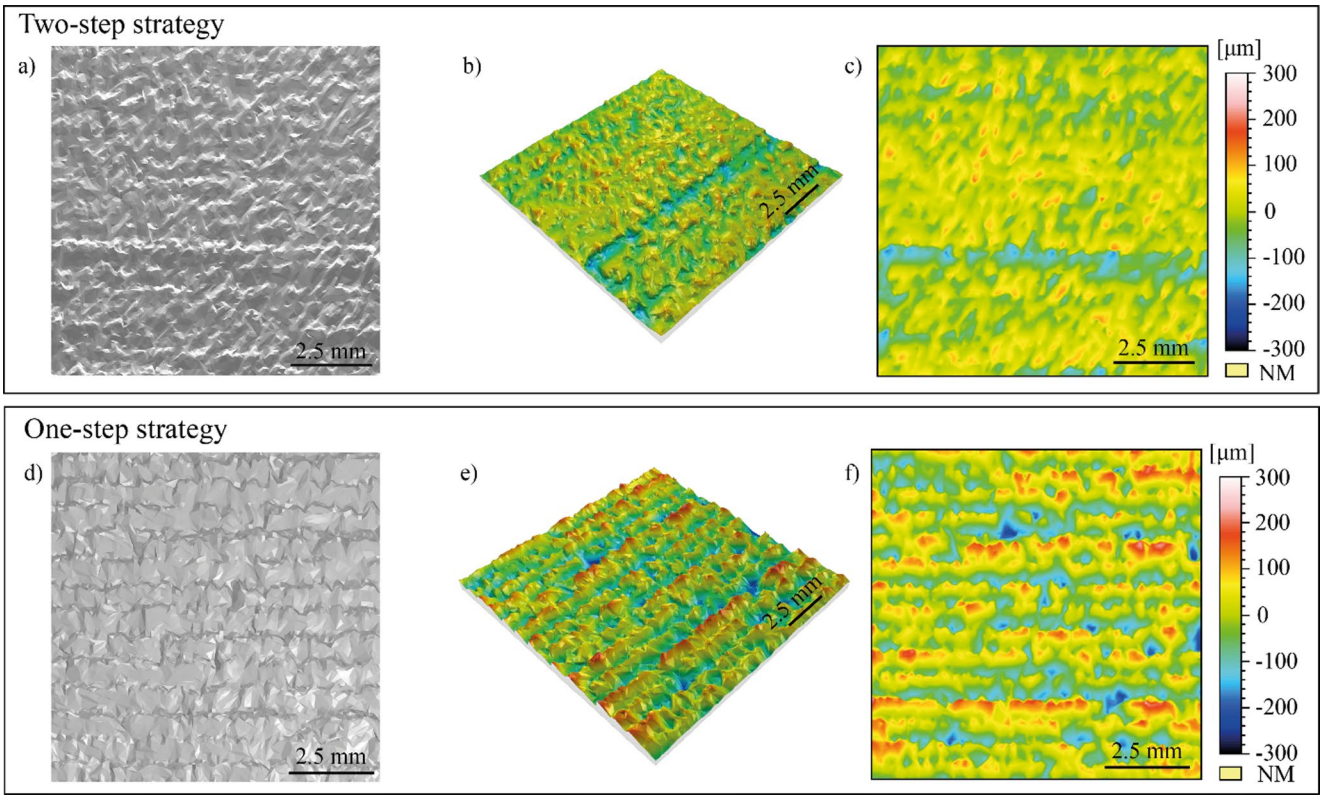

Fig. 6 Topography analysis of the vertical surfaces. **a**–**c** Refer to the surface produced with the two-step strategy, while **d**–**f** refer to the surface produced with the one-step strategy. **a**, **d** Represent the unprocessed STL file. **b**, **e** represent the 3D height map. **c**, **f** Represent the false colour height map

(Fig. 7a–c) and the one-step strategy (Fig. 7d–f) show the presence of parallel lines which correspond to the melt tracks. The similarity among the horizontal surfaces is also given by the similar values of average area roughness. For the surface produced using the two-step strategy Sa = 20 µm, while for the surface produced using the one-step strategy Sa = 22 µm.

The visible pattern on horizontal surfaces is the summary of several adjacent tracks that fill the inner section and partially overlap each other. This is shown in Fig. 8 for a horizontal surface of the sample produced with a one-step strategy. When the electron beam scans the powder bed, it forms a melt track: the cross-section of the melt track usually has a dome shape, characterised by a width and a height [41]. This shape depends on the interaction between the molten material and previously melted solid substrate. As shown in Fig. 8 a), each line is continuous without defects due to, e.g., the occurrences of balling, Rayleigh instability or unmelted particles. Continuous line proves that the process was stable during the production, ensuring homogeneity of the material [23]. The visible tracks are the result of a line which overlaps the previous one. Therefore, it does not represent the width of an actual melted line, which may vary between 300 µm [41] and 800 µm [42], depending on the material and the processing condition. On the other hand, the distance between two peaks of the pattern is a measure of the distance between the melt tracks, called line offset (LO). In this case, as measured in Fig. 8 b), this distance is 328 ± 22 µm, which is comparable to the set line offset (Table 2) adopted to melt the cross-section. This distance can be measured among the valleys that are visible on the false colour map in Fig. 7, which are formed at the intersection of two adjacent melt tracks.

3.2 Dimensional accuracy

The data for dimensional accuracy evaluation collected with the CMM are reported in a dataset 49. Figure 9 shows the number of tolerance units obtained from measuring the artefacts for the base ISO ranges considered in this work. The data compares the results of the one-step and two-step melting strategies. This study aims to highlight the capabilities of PBF-EB in processing Ti4822 using the selected process parameters. Therefore, the results should be interpreted as an assessment of the process's precision limits, where the IT grade achieved by each strategy for each size range represents the best attainable accuracy within the constraints of the manufacturing technique. For instance, if the process

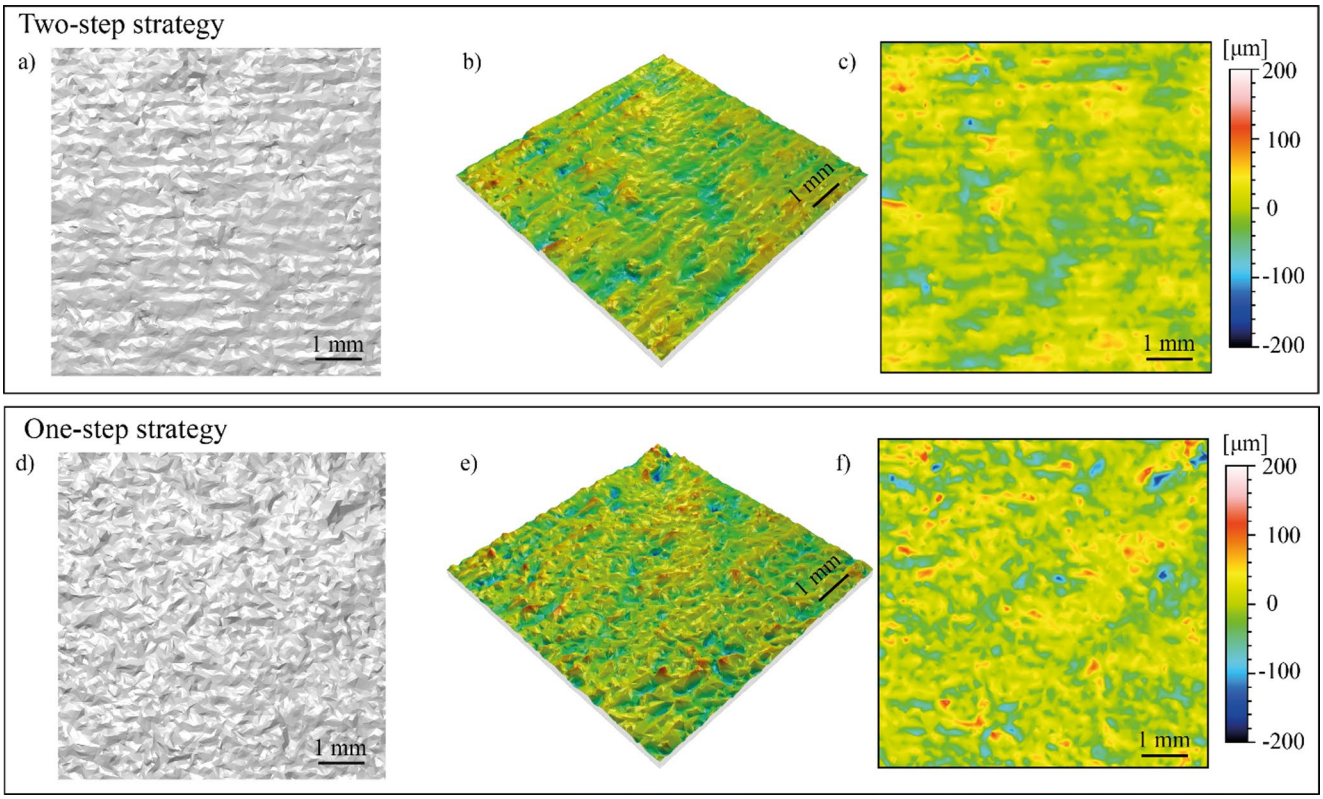

Fig. 7 Topography analysis of the horizontal surfaces. **a**–**c** refer to the surface produced with the two-step strategy, while **d**–**f** refer to surfaces produced with the one-step strategy. **a**, **d** Represent the unprocessed STL file. **b**, **e** represent the 3D height map. **c**, **f** represent the false colour height map

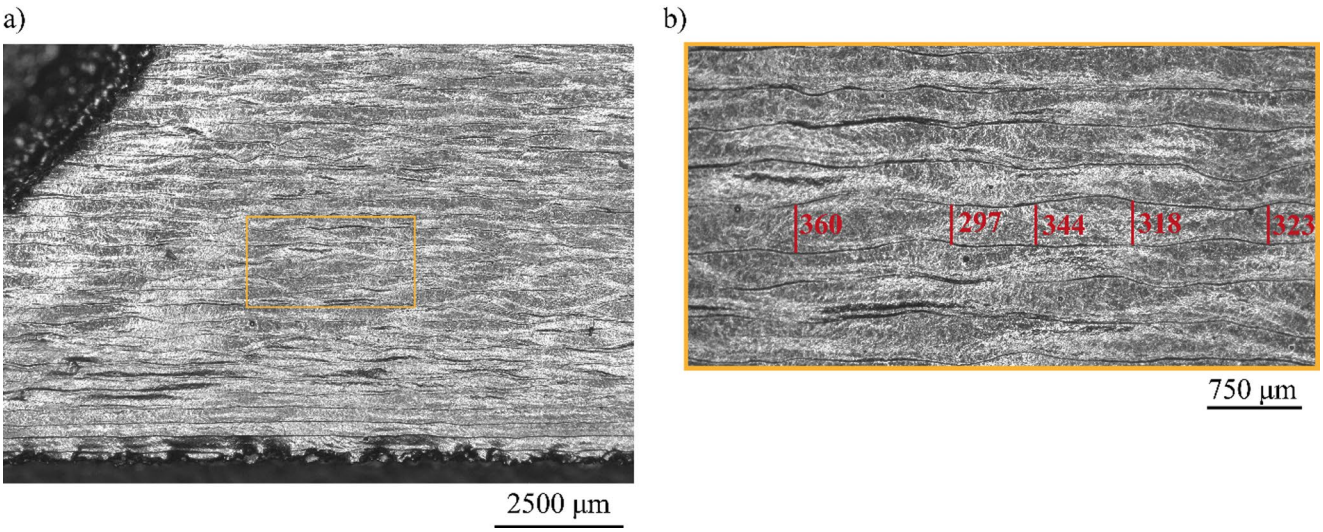

Fig. 8 **a)** Optical microscopy image of the top surface. **b)** Detail of the surface with measures of the width of the melt track in µm

can only achieve IT15 for a specific feature size, it indicates an inherent limitation of the PBF-EB for that feature, preventing the attainment of tighter tolerances such as IT7. In addition, it should be considered that no scaling factor has been applied to the geometry to account for geometrical error due to, e.g., the volume shrinkage.

Keeping this in mind and considering the number of tolerance units in all the basic ISO classes, the PBF-EB process for Ti4822 with the selected process parameters guarantees IT grades ranging from IT12 to IT16. The larger the feature of the sample, the higher the accuracy of the process (lower IT). For example, for the features comprising 1 mm and

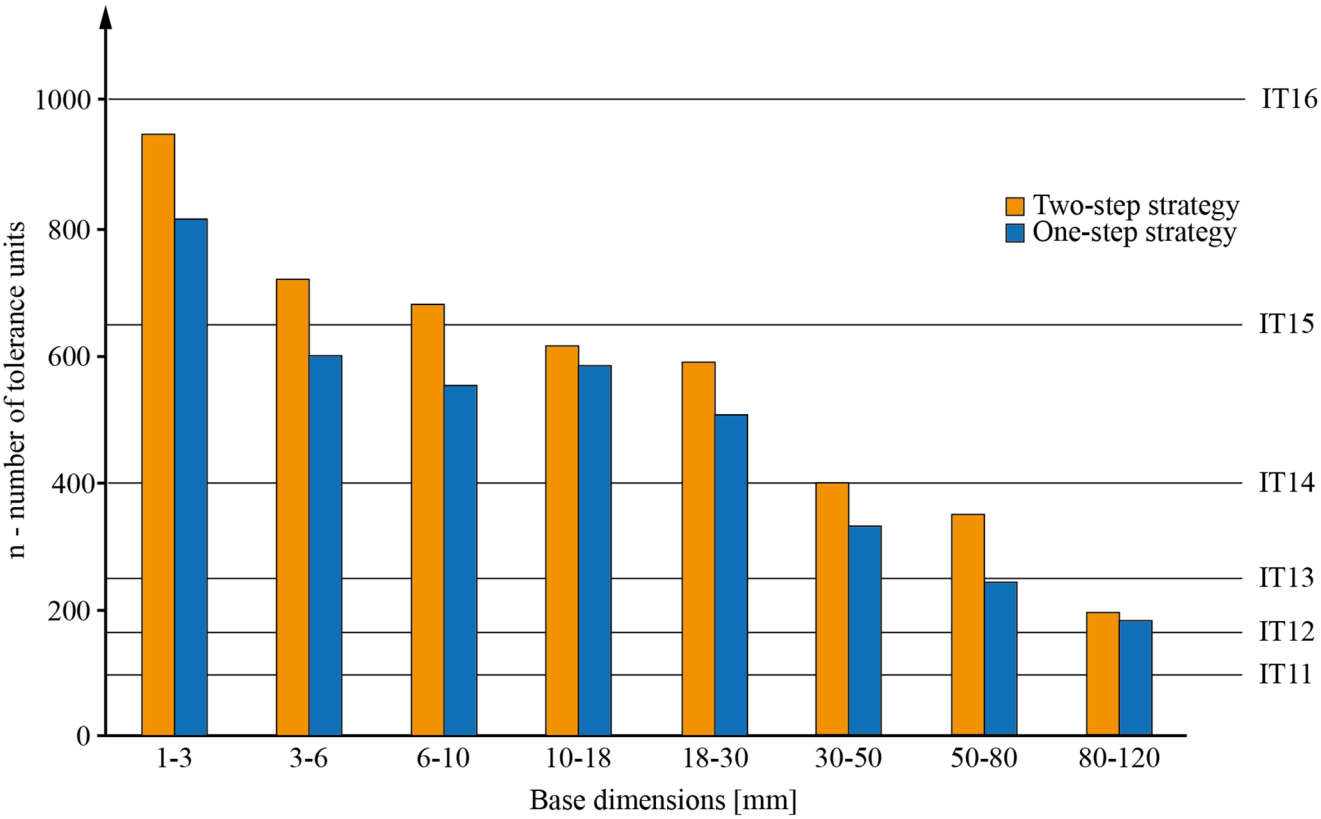

Fig. 9 Number of tolerance units for the artefacts produces using the Two-step strategy and the one-step strategy for the ISO base dimensions

Table 5 Tolerance width for the parts measured according to the ISO guidelines

Basic size [mm]	Tolerance width [mm] for the two-step strategy	Tolerance width [mm] for the one-step strategy
1–3	0.6 (IT16)	0.6 (IT16)
3–6	0.75 (IT16)	0.48 (IT15)
6–10	0.9 (IT16)	0.58 (IT15)
10–18	0.7 (IT15)	0.7 (IT15)
18–30	0.84 (IT15)	0.84 (IT15)
30–50	0.62 (IT14)	0.62 (IT14)
50–80	0.74 (IT14)	0.46 (IT13)
80–120	0.54 (IT13)	0.54 (IT13)

3 mm, the PBF-EB process can guarantee an IT 16, while for the larger features with dimensions from 80 to 120 mm, the PBF-EB process guarantees an IT 13. These values are comparable with processes such as casting [43], with which the PBF-EB technology is usually associated. The IT grades of the two melt strategies differ only for a few ISO classes. In particular, the samples produced with the one-step strategy have a higher dimensional accuracy (lower IT) than the samples produced with the two-step strategy for the classes 3–6 mm and 6–10 mm (two-step process guarantees an IT 16 while, the one-step strategy can guarantee an IT 15), and in the base range 50–80 mm, for which the two-step strategy guarantees an IT 14, while the one-step strategy guarantees an IT 13. However, it should be noted that the tolerance width [33, 34] of the measured IT grades for each specific ISO size class is overall similar among the ISO size classes (Table 5). The maximum value of the tolerance width is registered for the two-step strategy, and it is equal to 0.9 mm, which corresponds to the IT16 for the ISO size class from 6 to 10 mm. The minimum value is registered for the one-step strategy, and it is equal to 0.46 mm (IT13) for the ISO size class ranging from 50 to 80 mm. Although the variation could appear small, it should be noted that it depends on the dimension. Therefore, the application of a uniform scaling factor to the component independently of the feature dimension could be un insufficient corrective factor to adjust the dimension before the production.

In addition to the IT grade, which defines the width of the tolerance and although for some basic sizes the IT grade for the process is the same, the tolerance position should be considered because it specifies where the tolerance width is located in relation to the nominal dimension. Remarkably, the analysis of the acquired measurements shows that the melting strategy strongly affects the position of the tolerance band. As an example of this, a feature like a cylinder of CC1 of artefact 2 (Fig. 1b) is considered. The feature is a hollowed cylinder. Figure 10 schematically illustrates the

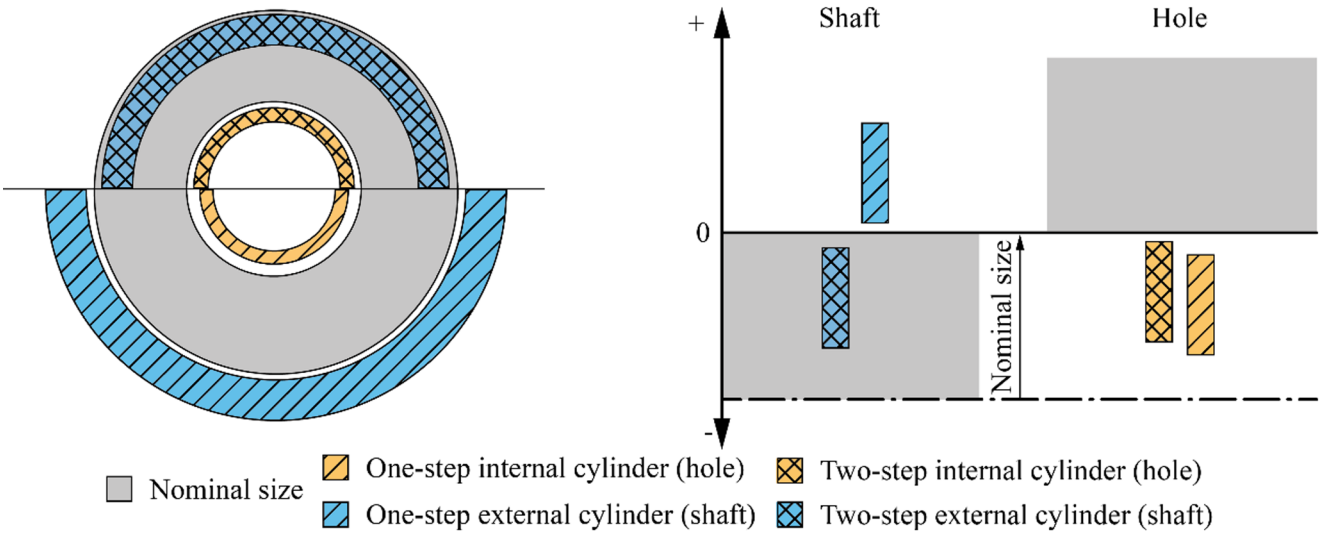

Fig. 10 Schematic representation of the tolerance interval and the relative position with respect to the nominal size. The dimensions are out of scale

position of the tolerance band relative to the nominal diameter of the inner and outer surfaces of the hollowed cylinder, represented in a shaft/hole configuration. The two-step strategy consistently produces external features (shaft) that are smaller than the nominal dimension, whereas the one-step strategy results in external features (shaft) that are always larger than the nominal.

For internal features (hole), both melting strategies yield dimensions smaller than the nominal. However, the position of the tolerance band differs between the two approaches. In some cases, the one-step strategy produces smaller internal features than those obtained with the two-step strategy. The beam trajectory may explain this effect. In the two-step strategy, the beam is expected to overlap the nominal contour of the part. However, due to the limited heat input associated with the multi-beam approach, the melt pool remains relatively small. Consequently, the reduced contour dimension compared to the nominal could be attributed to shrinkage. This effect may be mitigated by applying a larger contour offset (Table 2) to compensate for the shrinkage.

According to Table 5, it can be inferred that the contour offset should be at least half of the tolerance band height for the corresponding feature dimension. This finding may also provide an explanation for the necessity of applying a scaling factor [29, 44, 45], which is, however, typically independent of feature size and is determined as the best interpolation to prevent material loss.

The excess material observed in the one-step strategy can also be explained by the beam trajectory. In this case, the beam is expected to stop precisely at the part perimeter. However, the heat input during the melting of the hatching region generates a melt pool that, in some cases, is significantly larger than the beam diameter, leading to an excess of melted material in front of the melt pool. This excess is subsequently detected as the tolerance height. Notably, the obtained tolerance height values (see Table 5) are consistent with the typical melt pool width observed in PBF-EB [42, 46].

Overall, the one-step strategy is advantageous for finishing operations, as it inherently provides an excess of material without requiring additional allowances or scaling factors during the design phase. Conversely, external features produced using the two-step strategy require adjustments through additional parameters, such as contour offsets or extra material additions.

3.3 Geometrical tolerances

Figure 11 shows the geometrical tolerance results for planarity and parallelism in an aggregate form as a box plot. Considering both planarity and parallelism, the melting strategy does not have a statistically relevant effect on the dimensional accuracy since all the boxes overlap. However, the two-step strategy has a beneficial effect on the planarity of the vertical surfaces that shows a reduced median and interquartile range. The same applies to the parallelism of the vertical surfaces, where the vertical surfaces produced with a two-step strategy have a smaller median and an interquartile range below that of the vertical surface produced with the one-step strategy. These results agree with the results obtained from the topography analysis of vertical surfaces reported in Sect. 3.1. The difference in the dimensional accuracy among the melting strategies could be related to the larger peaks and valleys and larger values of surface roughness for vertical surfaces produced with the one-step strategy.

Figure 12 summarises the tolerance data for the perpendicularity, coaxiality and cylindricity as box plots for the two

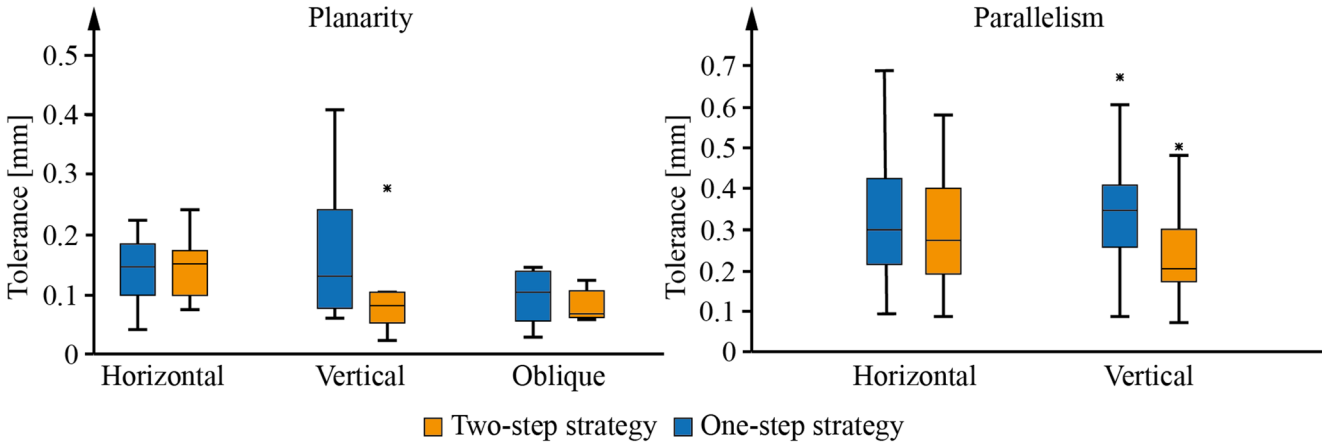

Fig. 11 Geometrical tolerances for planarity and parallelism

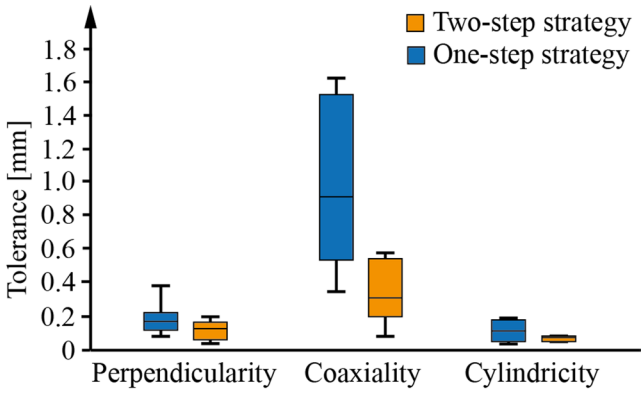

Fig. 12 Tolerance for Perpendicularity, coaxiality and cylindricity in the case of the two melting strategies

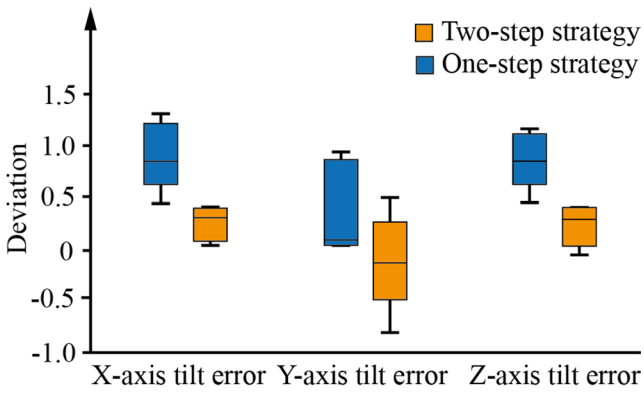

Fig. 13 Deviation of the angles with respect to the coordinate axes for the two-step and one-step melting strategy considered

melt strategies. The box plot shows that the melting strategy is not statistically relevant on the perpendicularity, coaxiality and cylindricity. Regarding the coaxiality, although the overlapping of the boxes, the median and the interquartile range obtained for the features produced using the two-step strategy are smaller than those produced using the two-step strategy. This means that, on average, the two-step strategy produced better coaxiality of the features.

Figure 13 shows the box plots for the tilt angles of the surfaces with respect to the coordinate axes defined in Fig. 2. In this case, for the deviation with respect to the X-axis and the deviation with respect to the Z-axis, the melting strategy is statistically relevant. The two-step strategy produces surfaces tilted with a smaller deviation with respect to the coordinate axes. On the other hand, the melting strategy does not have a statistically relevant effect on the deviation of the tilt angle with respect to the Y-axis. While the interquartile range is comparable for the two-step and the one-step strategy, the median of the two-step strategy is smaller, and the box shows smaller deviation values. However, the interquartile range for surfaces produced with the two-step strategy goes at negative values, while this never happens for surfaces produced with the one-step strategy.

The box plots of the geometrical tolerances indicate that the melting strategy does not induce strong variations in the overall geometrical accuracy of the parts. Nevertheless, some systematic effects can be identified. In particular, features such as the planarity of vertical surfaces, coaxiality and deviation of the tilt angle exhibit smaller deviations when processed with the two-step strategy. The most pronounced differences between the two melting approaches arise for surfaces that deviate from the horizontal, those whose accuracy is governed by the stability of nearly vertical walls. This difference can be explained by the thermal boundary conditions at the start and end of each melt track. In the one-step approach, the hatching lines begin and terminate on sintered powder. Owing to the considerably lower thermal conductivity of the powder bed compared to consolidated material, heat accumulates locally at the melt pool boundaries, promoting higher thermal gradients and subsequent shrinkage during solidification. As a result, the external surfaces are more prone to inward distortion, which

can increase the deviation from the nominal geometry. In contrast, when a contour is performed prior to hatching, the melt tracks start and end on a solid region that provides a more efficient heat transfer path. This reduces overheating at the melt pool edges and mitigates localised shrinkage, therefore improving dimensional stability along the component borders. These findings agree with Ref. [47]. This effect becomes more pronounced with increasing build height, as the thermal stabilising influence of the start plate progressively diminishes [48]. The resulting differences in thermal behaviour from the bottom to the top of the part can rationalise the lower geometrical accuracy and the larger deviations in tilt angle observed for components produced with the one-step strategy. Additionally, the greater dispersion observed in the parallelism of vertical surfaces (Fig. 11) may be attributed to the higher surface roughness generated by the one-step strategy, which affects the reliability of contact-based CMM probing and thus increases the spread of measured values.

4 Conclusions

The building conditions of the powder bed fusion with electron beam (PBF-EB) additive manufacturing process enable the easier processing of the γ-TiAl Ti48Al2Cr2Nb than other manufacturing processes. This alloy has extensive applications in aerospace and good potentialities for other fields such as biomedical and automotive. For practical applications, knowledge about topology, dimensional and geometrical accuracy is fundamental for manufacturing feasibility, cost control and quality assurance. If the required accuracy is within the process capability, the part can be made directly to size, reducing costs or accurately planning subsequent machining operations. This study examines the influence of one-step and two-step melting strategies in PBF-EB processing of Ti4822, focusing on surface topography and dimensional accuracy. The findings reveal that the choice of melting strategy significantly affects surface roughness and contour definition, particularly on vertical surfaces.

The two-step strategy produces smoother surfaces with a reduced stair-stepping effect, as evidenced by lower Sa and Sz values compared to the one-step approach. This improvement is attributed to the presence of a solid contour in the two-step strategy, which reduces material accumulation at the tail of the melt pool. Despite these differences, both strategies exhibit periodic patterns on vertical surfaces, likely due to hatch direction rotation and comparable topographical characteristics on horizontal surfaces, where melt tracks remain continuous and defects-free.

Dimensional accuracy analysis shows that PBF-EB of Ti4822 can achieve IT grades ranging from IT12 to IT16, with larger features generally exhibiting higher precision. While both strategies yield similar tolerance bands, the one-step approach offers slightly improved dimensional accuracy for specific size ranges. On the other hand, the tolerance band positioning differs between strategies. The two-step strategy consistently produces external features smaller than the nominal dimension, whereas the one-step strategy results in external features larger than the nominal. Internal features in both cases tend to be undersized. Since the two-step strategy consistently produces components smaller than the nominal design, it needs compensatory adjustments in the CAD model, such as applying a scale factor. However, a uniform scale factor may not suffice, as accuracy and tolerance height depend on feature dimensions. Alternatively, processing parameters can be adjusted by applying a contour offset, allowing the beam to melt a contour slightly offset from the nominal design. This approach can compensate for material shrinkage during cooling, improving dimensional accuracy.

In addition to these dimensional considerations, it should be considered that the two-step strategy requires, on average, 8% more processing time than the one-step approach. Therefore, this strategy with the proper correction, e.g. considering post heat treatment of the material, may be used to produce components in such fields, e.g. biomedical, in which the measured roughness in the as-built condition is already adequate for the application. For features of components that require post-processing, such as those in the aerospace or automotive sectors, the one-step melting strategy is recommended because the tolerance band positioning ensures that components are consistently larger than the nominal dimensions, providing extra material for subsequent finishing operations.

As regards geometrical accuracy, the two-step strategy was shown to produce slightly more accurate features. However, the effect is limited and geometrical accuracy can be considered as a secondary decisional parameter about which melt strategy to adopt.

These findings highlight the importance of selecting an appropriate melting strategy based on surface quality and dimensional precision requirements. These preliminary results are intended to be used as guidelines to help decide whether the PBF-EB process alone can meet the required tolerances or if additional machining is necessary. Since IT grades vary with size, small features (e.g., holes and thin walls) might require tighter compensation than large bulk features. This means that the compensation should be tailored to the tolerance requirement for each feature, rather than applying a uniform shrinkage factor. If the required IT grade is tight, machining is needed. Knowing the IT grade

allows for adding the minimum sufficient extra material to critical surfaces for final machining. The application of such results is also intended to be used as information in simulation tools to suggest a corrected/adjusted geometry that, during the production, may compensate for the deviations of the process.

Acknowledgements Carmelo Daniele Delacqua for the help in acquiring the digital model with the structured light scanner and Salvatore Varvieri for the help with the dimensional measures with the CMM are gratefully acknowledged.

Author contributions Conceptualisation, M.G. and P.M.; data curation, G.R.; formal analysis, G.R.; investigation, G.R. and M.G.; methodology, M.G. and P.M.; resources, M.G.; software, P.M., G.R.; supervision, M.G.; visualisation, G.R.; writing—original draft, G.R.; writing—review and editing, M.G. and P.M.

Funding Open access funding provided by Politecnico di Torino within the CRUI-CARE Agreement.

Data availability The details regarding sample characterization are thoroughly reported. The STL file of the geometry of the artefact can be downloaded for free. A dataset with free online access containing all the dimensional measurements is available on line 49.

Declarations

Competing interests The authors declare no competing interests.

Open Access This article is licensed under a Creative Commons Attribution 4.0 International License, which permits use, sharing, adaptation, distribution and reproduction in any medium or format, as long as you give appropriate credit to the original author(s) and the source, provide a link to the Creative Commons licence, and indicate if changes were made. The images or other third party material in this article are included in the article's Creative Commons licence, unless indicated otherwise in a credit line to the material. If material is not included in the article's Creative Commons licence and your intended use is not permitted by statutory regulation or exceeds the permitted use, you will need to obtain permission directly from the copyright holder. To view a copy of this licence, visit http://creativecommons.org/licenses/by/4.0/.

References

1. Chen W, Li Z (2019) 11—additive manufacturing of titanium aluminides. In: Froes F, Boyer R (eds) Additive manufacturing for the aerospace industry. Elsevier, New York, pp 235–263
2. Wartbichler R, Clemens H, Mayer S et al (2021) On the formation mechanism of banded microstructures in electron beam melted Ti–48Al–2Cr–2Nb and the design of heat treatments as remedial action. Adv Eng Mater 23:2101199. https://doi.org/10.1002/adem.202101199
3. Galati M (2021) Chapter 8 - electron beam melting process: a general overview. In: Pou J, Riveiro A, Davim JP (eds) Additive manufacturing. Elsevier, New York, pp 277–301
4. Sinha A, Swain B, Behera A et al (2022) A review on the processing of aero-turbine blade using 3D print techniques. J Manuf Mater Process 6:16. https://doi.org/10.3390/jmmp6010016
5. Galati M, Gatto ML, Bloise N et al (2024) Electron beam powder bed fusion of Ti-48Al-2Cr-2Nb open porous scaffold for biomedical applications: process parameters, adhesion, and proliferation of NIH-3T3 cells. 3D Print Addit Manuf 11:314–322. https://doi.org/10.1089/3dp.2022.0108
6. Larsson M, Snis A (2012) Method and device for producing three-dimensional objects
7. Bieske J, Franke M, Schloffer M, Körner C (2020) Microstructure and properties of TiAl processed via an electron beam powder bed fusion capsule technology. Intermetallics 126:106929. https://doi.org/10.1016/j.intermet.2020.106929
8. Kurzynowski T, Madeja M, Dziedzic R, Kobiela K (2019) The effect of EBM process parameters on porosity and microstructure of Ti-5Al-5Mo-5V-1Cr-1Fe alloy. Scanning 2019:2903920. https://doi.org/10.1155/2019/2903920
9. Rizza G, Galati M (2024) Powder bed fusion with electron beam: the interplay of sintering, porosity, and coordination number in modelling the powder thermal conductivity through a novel tortuosity formulation. Int J Heat Mass Transf 234:126055. https://doi.org/10.1016/j.ijheatmasstransfer.2024.126055
10. Panin PV, Lukina EA, Bogachev IA, Naprienko SA (2023) Effect of technological parameters of selective electron beam melting on chemical composition, microstructure, and porosity of a TiAl-alloy of Ti-Al-V-Nb-Cr-Gd system. Metallurgist 67:628–643. https://doi.org/10.1007/s11015-023-01551-y
11. Tao H, Li H, Li J et al (2024) Tensile creep of an additively manufactured Ti-48Al-2Cr-2Nb alloy with a layered microstructure. Mater Sci Eng A 916:147288. https://doi.org/10.1016/j.msea.2024.147288
12. Baudana G, Biamino S, Klöden B et al (2016) Electron beam melting of Ti-48Al-2Nb-0.7Cr-0.3Si: feasibility investigation. Intermetallics 73:43–49. https://doi.org/10.1016/j.intermet.2016.03.001
13. Chen Y, Yue H, Wang X (2018) Microstructure, texture and tensile property as a function of scanning speed of Ti-47Al-2Cr-2Nb alloy fabricated by selective electron beam melting. Mater Sci Eng A 713:195–205. https://doi.org/10.1016/j.msea.2017.12.020
14. Cormier D, Harrysson O, Mahale T, West H (2007) Freeform fabrication of titanium aluminide via electron beam melting using prealloyed and blended powders. Res Lett Mater Sci 2007:34737. https://doi.org/10.1155/2007/34737
15. Todai M, Nakano T, Liu T et al (2017) Effect of building direction on the microstructure and tensile properties of Ti-48Al-2Cr-2Nb alloy additively manufactured by electron beam melting. Addit Manuf 13:61–70. https://doi.org/10.1016/j.addma.2016.11.001
16. Murr LE, Gaytan SM, Ceylan A et al (2010) Characterization of titanium aluminide alloy components fabricated by additive manufacturing using electron beam melting. Acta Mater 58:1887–1894. https://doi.org/10.1016/j.actamat.2009.11.032
17. Mohammad A, Alahmari AM, Mohammed MK et al (2017) Effect of energy input on microstructure and mechanical properties of titanium aluminide alloy fabricated by the additive manufacturing process of electron beam melting. Materials 10:211. https://doi.org/10.3390/ma10020211
18. Kim Y-K, Youn S-J, Kim S-W et al (2019) High-temperature creep behavior of gamma Ti-48Al-2Cr-2Nb alloy additively manufactured by electron beam melting. Mater Sci Eng A 763:138138. https://doi.org/10.1016/j.msea.2019.138138
19. Schwerdtfeger J, Körner C (2014) Selective electron beam melting of Ti–48Al–2Nb–2Cr: microstructure and aluminium loss. Intermetallics 49:29–35. https://doi.org/10.1016/j.intermet.2014.01.004
20. Körner C (2016) Additive manufacturing of metallic components by selective electron beam melting—a review. Int Mater Rev 61:361–377. https://doi.org/10.1080/09506608.2016.1176289

21. Wang P, Sin WJ, Nai MLS, Wei J (2017) Effects of processing parameters on surface roughness of additive manufactured Ti-6Al-4V via electron beam melting. Materials 10:1121. https://doi.org/10.3390/ma10101121
22. Galati M, Rizza G, Defanti S, Denti L (2021) Surface roughness prediction model for electron beam melting (EBM) processing Ti6Al4V. Precis Eng 69:19–28. https://doi.org/10.1016/j.precisioneng.2021.01.002
23. Galati M, Defanti S, Saboori A et al (2022) An investigation on the processing conditions of Ti-6Al-2Sn-4Zr-2Mo by electron beam powder bed fusion: microstructure, defect distribution, mechanical properties and dimensional accuracy. Addit Manuf 50:102564. https://doi.org/10.1016/j.addma.2021.102564
24. Zhao X, Rashid A, Dadbakhsh S (2019) Influence of contouring and depth of machining on tensile properties of inconel 625 made by electron beam melting, pp 118–127
25. Cormier D, Harrysson O, West H (2004) Characterization of H13 steel produced via electron beam melting. Rapid Prototyping J 10:35–41. https://doi.org/10.1108/13552540410512516
26. Pirozzi C, Franchitti S, Borrelli R et al (2019) Experimental study on the porosity of electron beam melting-manufactured Ti6Al4V. J Mater Eng Perform 28:2649–2660. https://doi.org/10.1007/s11665-019-04038-7
27. Karimi P, Schnur C, Sadeghi E, Andersson J (2020) Contour design to improve topographical and microstructural characteristics of alloy 718 manufactured by electron beam-powder bed fusion technique. Addit Manuf 32:101014. https://doi.org/10.1016/j.addma.2019.101014
28. Cooke AL, Soons JA (2010) Variability in the geometric accuracy of additively manufactured test parts. University of Texas, Austin
29. Smith CJ, Derguti F, Hernandez Nava E et al (2016) Dimensional accuracy of electron beam melting (EBM) additive manufacture with regard to weight optimized truss structures. J Mater Process Technol 229:128–138. https://doi.org/10.1016/j.jmatprotec.2015.08.028
30. Bol E, Ramulu M (2023) Dimensional accuracy of electron beam powder bed fusion with Ti-6Al-4V. Designs 7:53. https://doi.org/10.3390/designs7020053
31. Camilleri C, Rochman A (2019) Defect formation in EBM parts built at different orientation. J Adv Technol Eng Res 5:125–134. https://doi.org/10.20474/jater-5.3.3
32. Minetola P, Iuliano L, Marchiandi G (2016) Benchmarking of FDM machines through part quality using IT grades. Procedia CIRP 41:1027–1032. https://doi.org/10.1016/j.procir.2015.12.075
33. (1988) ISO 286:1988 ISO system of limits and fits. Part 1 bases of tolerances deviations and fits
34. (2010) BS EN ISO 286-1:2010 geometrical product specifications (GPS). ISO code system for tolerances on linear sizes. Basis of tolerances, deviations and fits
35. Minetola P, Galati M, Calignano F et al (2020) Comparison of dimensional tolerance grades for metal AM processes. Procedia CIRP 88:399–404. https://doi.org/10.1016/j.procir.2020.05.069
36. Minetola P, Calignano F, Galati M (2020) Comparing geometric tolerance capabilities of additive manufacturing systems for polymers. Addit Manuf 32:101103. https://doi.org/10.1016/j.addma.2020.101103
37. Galati M, Minetola P (2019) Analysis of density, roughness, and accuracy of the atomic diffusion additive manufacturing (ADAM) process for metal parts. Materials 12:4122. https://doi.org/10.3390/ma12244122
38. Benchmarking of additive technologies | 3D CAD model library | GrabCAD. https://grabcad.com/library/benchmarking-of-additive-technologies-1. Accessed 2 Feb 2025
39. Biamino S, Penna A, Ackelid U et al (2011) Electron beam melting of Ti-48Al-2Cr-2Nb alloy: microstructure and mechanical properties investigation. Intermetallics 19:776–781. https://doi.org/10.1016/j.intermet.2010.11.017
40. Schindelin J, Arganda-Carreras I, Frise E et al (2012) Fiji: an open-source platform for biological-image analysis. Nat Methods 9:676–682. https://doi.org/10.1038/nmeth.2019
41. Galati M, Snis A, Iuliano L (2019) Powder bed properties modelling and 3D thermo-mechanical simulation of the additive manufacturing electron beam melting process. Addit Manuf 30:100897. https://doi.org/10.1016/j.addma.2019.100897
42. Karimi P, Sadeghi E, Ålgårdh J, Andersson J (2019) EBM-manufactured single tracks of alloy 718: influence of energy input and focus offset on geometrical and microstructural characteristics. Mater Charact 148:88–99. https://doi.org/10.1016/j.matchar.2018.11.033
43. Grazia Violante M, Iuliano L, Minetola P (2007) Design and production of fixtures for free-form components using selective laser sintering. Rapid Prototyping J 13:30–37. https://doi.org/10.1108/13552540710719190
44. Borrelli R, Franchitti S, Pirozzi C et al (2020) Ti6Al4V parts produced by electron beam melting: analysis of dimensional accuracy and surface roughness. J Adv Manuf Syst. https://doi.org/10.1142/S0219686720500067
45. Franchitti S, Borrelli R, Pirozzi C et al (2018) Investigation on electron beam melting: dimensional accuracy and process repeatability. Vacuum 157:340–348. https://doi.org/10.1016/j.vacuum.2018.09.007
46. Galati M, Snis A, Iuliano L (2019) Experimental validation of a numerical thermal model of the EBM process for Ti6Al4V. Comput Math Appl 78:2417–2427. https://doi.org/10.1016/j.camwa.2018.07.020
47. Zhao X, Rashid A, Strondl A et al (2021) Role of superficial defects and machining depth in tensile properties of electron beam melting (EBM) made inconel 718. J Mater Eng Perform 30:2091–2101. https://doi.org/10.1007/s11665-021-05487-9
48. Landau E, Tiferet E, Ganor YI et al (2020) Thermal characterization of the build chamber in electron beam melting. Addit Manuf 36:101535. https://doi.org/10.1016/j.addma.2020.101535
49. Rizza G, Minetola P, Galati M et al (2025) Dimensional and geometrical data of artefacts produced with PBF-EB in Ti4822 alloy, Mendeley Data, V2, https://doi.org/10.17632/k5f2fnggsc.2

Publisher's Note Springer Nature remains neutral with regard to jurisdictional claims in published maps and institutional affiliations.